Evolution of Marine Atmospheric Boundary Layer Structure across the Cold Tongue–ITCZ Complex

HOLLIS E. PYATT AND BRUCE A. ALBRECHT

Division of Meteorology and Physical Oceanography, Rosenstiel School of Marine and Atmospheric Science, University of Miami, Miami, Florida

CHRIS FAIRALL AND J. E. HARE

NOAA/ETL, Boulder, Colorado

NICHOLAS BOND

JISAO/University of Washington, Seattle, Washington

PATRICK MINNIS

Atmospheric Sciences Division, NASA Langley Research Center, Hampton, Virginia

J. KIRK AYERS

Analytical Sciences and Materials, Inc., Hampton, Virginia

(Manuscript received 22 April 2004, in final form 30 August 2004)

ABSTRACT

The structure of the marine atmospheric boundary layer (MABL) over the tropical eastern Pacific Ocean is influenced by spatial variations of sea surface temperature (SST) in the region. As the MABL air is advected across a strong SST gradient associated with the cold tongue–ITCZ complex (CTIC), substantial changes occur in the thermodynamic structure, surface fluxes, and cloud properties. This study attempts to define and explain the variability in the MABL structure and clouds over the CTIC. Using data collected on research cruises from the fall seasons of 1999–2001, composite soundings were created for both the cold and warm sides of the SST front to describe the mean atmospheric boundary layer (ABL) structure and its evolution across this front. The average difference in SST across this front was ~6°C; much of this difference was concentrated in a band only ~50 km wide. During the fall seasons, on the cold side of the gradient, a well-defined inversion exists in all years. Below this inversion, both fair-weather cumulus and stratiform clouds are observed. As the MABL air moves over the SST front to warmer waters, the inversion weakens and increases in height. The MABL also moistens and eventually supports deeper convection over the ITCZ. Both the latent and sensible heat fluxes increase dramatically across the SST front because of both an increase in SST and surface wind speed. Cloudiness is variable on the cold side of the SST front ranging from 0.2 to 0.9 coverage. On the warm side, cloud fraction was quite constant in time, with values generally greater than 0.8. The highest cloud-top heights (>3 km) are found well north of the SST front, indicating areas of deeper convection. An analysis using energy and moisture budgets identifies the roles of various physical processes in the MABL evolution.

1. Introduction and background

The atmospheric boundary layer can be defined as "that part of the troposphere that is directly influenced by the presence of the earth's surface, and responds to surface forcings with a timescale of about an hour or less" (Stull 1988). The marine atmospheric boundary layer (MABL) over the earth's oceans plays a critical role in regulating the surface energy and moisture fluxes and in controlling the convective transfer of energy and moisture to the free atmosphere (Kloesel and Albrecht 1989). Generally over the oceans, Lagrangian changes in the structure of the MABL are modest because the MABL is in quasi equilibrium with the sea surface temperatures (SSTs; Stull 1988). There exist

Corresponding author address: Dr. Bruce A. Albrecht, Division of Meteorology and Physical Oceanography, Rosenstiel School of Marine and Atmospheric Science, University of Miami, 4600 Rickenbacker Causeway, Miami, FL 33149.
E-mail: balbrecht@rsmas.miami.edu

© 2005 American Meteorological Society

some areas of the earth's oceans, however, where strong gradients in SST can be found. One of these areas is the tropical eastern Pacific Ocean and is known as the cold tongue–ITCZ complex (CTIC). Figure 1 shows Tropical Rainfall Measuring Mission (TRMM) Microwave Imager (TMI) satellite estimates of SST for 14–16 November 1999; both the cold tongue and strong SST gradient or equatorial front are quite distinct. As the MABL is advected from the cooler waters of the cold tongue across the equatorial front toward warmer waters, the structure of the boundary layer changes dramatically. Clouds such as fair-weather cumulus and stratocumulus are often present in the MABL with general increases in cloudiness on the warm side of the equatorial front (Deser et al. 1993). The presence of these clouds substantially affects the radiation balance of the ocean surface by decreasing the amount of solar radiation absorbed in the ocean's mixed layer with little change in thermal radiation emitted to space (Albrecht et al. 1995). Several studies have provided evidence that these MABL clouds can strongly influence the earth's climate, and thus a realistic representation of these clouds is necessary for realistic model simulations (Albrecht et al. 1995).

Over the eastern equatorial Pacific, there have been relatively few observational studies of MABL structure and cloudiness. Wallace et al. (1989) focused on both the seasonal and interannual variability in the eastern Pacific Ocean using about 40 yr of data. In evaluating the seasonal and interannual variability, Wallace et al. found that the greatest variability in SST was around 1°S, in the vicinity of the cold tongue. Wallace et al. hypothesized that as air flows northward over the cold tongue, it becomes stably stratified (air temperatures are warmer than the SST). Because of the high stability, vertical mixing is inhibited, which leads to lower surface wind speeds and higher surface relative humidities over the cold tongue region, an effect that is especially true during the cold season of a cold year. As the air passes over the oceanic front where there is a large gradient in SSTs, the boundary layer becomes more unstable (the SSTs become warmer than the air temperatures); thus, the surface wind increases and the relative humidity decreases.

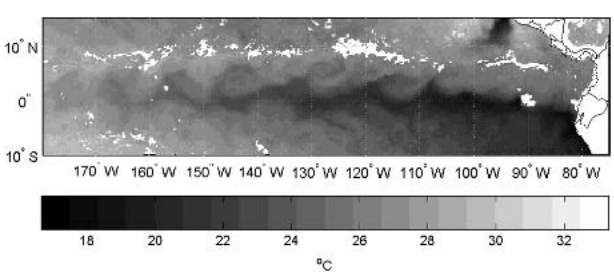

FIG. 1. TMI satellite-measured SST, 14–16 Nov 1999. The dark area (cooler SST) extending from the South American coast is the cold tongue. The undulations along the cold tongue are caused by westward-propagating tropical instability waves.

Bond's (1992) study of MABL structure in the eastern equatorial Pacific tests the hypothesis of Wallace et al. (1989) using data from nine days in October and November of 1989 along 110°W. Composite soundings were created for the cold tongue region (2°S–1°N) and also for 1.5°–6.5°N for this study. In the composite sounding located farther to the south, a slightly stable mixed layer existed with a more stable layer above. The surface layer shear in the meridional component (v) was stronger than in the zonal component (u). The composite sounding to the north had neutral stability from the top of the surface layer to about 600 m, with a greater specific humidity (q) than the sounding to the south. There was also little shear in either u or v. The results of this study are generally consistent with the findings of Wallace et al. (1989).

Yin and Albrecht (2000) used observations from the First Global Atmospheric Research Programme (GARP) Global Experiment (FGGE) to determine the structure and frequency of the trade inversion and transition-layer (a layer near cloud base where the mixing ratio decreases sharply and θ increases) structures in the tropical Pacific, as well as to look at the variation of the boundary layer across the CTIC. East–west cross sections for the cold tongue and ITCZ regions were created to examine boundary layer variability between these areas. Over the cold tongue, the air was drier than over the ITCZ, which had a relatively moist surface layer. This dryness over the cold tongue could be related to subsidence due to deep convection over the ITCZ or southeast trade winds blowing over the cold tongue. Over the ITCZ, the air was warmer from the surface to 800 hPa than over the cold tongue region; however, the air at 800 hPa over the cold tongue was slightly warmer than over the ITCZ. Yin and Albrecht (2000) developed north–south cross sections using the May–June 1979 data from 95° to 105°W. The main area of convection occurred from 8° to 10°N in the eastern equatorial Pacific, and the cold tongue was centered at 0°–2°S. There was an increase in moisture from south to north and a dry area at 800 hPa (above the MABL) at the equator. This dry area corresponds to a minimum in θ_e at the same location. One possible source of this dry air could be subsidence in response to upward motion in the ITCZ; another possibility is dry air protruding from the South American continent. The meridional wind increases in magnitude from 10°S to 7.5°N in the northward direction and then switches to southward and decreases in magnitude dramatically.

A recent study of the atmospheric boundary layer response to SST variations due to tropical instability waves (TIWs) over the eastern equatorial Pacific by Hashizume et al. (2002) has shown that the influence of the TIWs extends through the entire boundary layer. Inversion heights varied with TIW-induced SST changes—increasing over warmer SST and decreasing over cooler SST. During the TIW warm phase, a relatively deep cloud layer was observed above a surface

mixed layer with weakly stable stratification. During the cold TIW phase, there was a decoupling of the upper MABL from the mixed layer. The data also support the vertical-mixing mechanism hypothesized by both Wallace et al. (1989) and Hayes et al. (1989). Analysis of composites over warm SSTs shows that the zonal wind shear decreases over warm SSTs, which results in accelerated easterlies at the surface. Over cold SSTs, the zonal wind shear increases; thus, a decrease in easterlies in the MABL also occurs.

The purpose of this study is to define and explain the evolution of the MABL over the CTIC in terms of thermodynamics, surface fluxes, and cloud properties. Interannual variations in the boundary layer structure and its evolution will also be explored. Better understanding of this boundary layer evolution could eventually lead to the correction of deficiencies that currently exist in coupled models of the eastern Pacific ocean–atmosphere system (Weller 1999). Section 2 describes the data used in this study and the analysis methods employed. The general characteristics of the CTIC region for the fall season will then be described in section 3, followed by a detailed description of the MABL evolution in section 4. In section 5, energy and moisture budgets will be used to evaluate the role that various physical processes play in the MABL evolution. A summary is given in section 6.

2. Experiment and data

This study uses data collected on research cruises conducted as a part of the Eastern Pacific Investigation of Climate Processes in the Coupled Ocean–Atmosphere System (EPIC) study (Cronin et al. 2002). The National Oceanic and Atmospheric Administration (NOAA) ship *Ronald H. Brown* (*RHB*) completed two transects along 95° and 110°W in the eastern Pacific Ocean from 12°N to 8°S during each of the fall seasons of 1999–2001 for a total of six transects for the fall seasons (Fig. 2). This study will focus on the data collected along the 95°W transect since the CTIC characteristics are most prominent at this longitude.

Several types of data were collected during the transects. Soundings were taken every 6 h for an average total of about 30 per transect. These soundings were then used to calculate vertical profiles of thermodynamic variables such as potential temperature (θ), equivalent potential temperature (θ_e), and saturated equivalent potential temperature (θ_{es}) [calculations were made following Bolton (1980)]. Surface measurements of variables such as air temperature (T_a), specific humidity (q), wind speed, and SST were measured and logged by three shipboard systems: the Environmental Technology Laboratory (ETL) sonic anemometer with a sampling rate of 21.83 Hz, the ship's scientific computer system (SCS) that took data every 2 s, and the ETL mean measurement system that sampled meteorological parameters every 16 s. The shipboard observations were averaged to provide 5-min values of all variables. Air temperature and humidity measurements are a combination of ETL (aspirated Väisälä HMP-235) and Improved Meteorology (IMET; aspirated Rotronic) values. Sensible and latent heat fluxes were calculated from the shipboard data by applying a bulk flux parameterization (Fairall et al. 2003). These data were then smoothed using 1–2–1 averages to minimize smaller-scale variability. A ceilometer (Väisälä CT25K) provided observations of cloud-base height and cloudiness. Cloud properties, including cloud amount, height, and microphysical parameters, were derived from 4-km multispectral imager data taken hourly by the eighth Geostationary Operational Environmental Satellite over a large domain (Ayers et al. 2002) using the methodology of Minnis et al. (2001). A subset of the larger dataset between 15°N and 10°S was averaged into daily means corresponding to each of the cruise days for each subregion defined by 1° of latitude and 5° of longitude centered at 95°W.

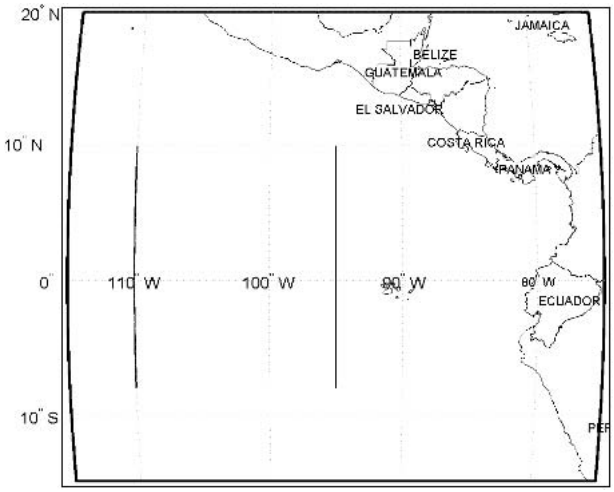

FIG. 2. Approximate track of research vessel during cruises from 1999 to 2001.

The Tropical Atmosphere Ocean (TAO) project buoy array extends across the 95°W meridian. Data available from these buoys include SST, air temperature, relative humidity, wind direction, and wind speed. Averages, as well as standard deviations of daily data, were calculated from each buoy for the above variables and were used to create cross sections along each meridian for the duration of each cruise. Latent and sensible heat fluxes were also calculated from the buoy data using the bulk aerodynamic method. The TAO data can be compared with the shipboard measurements to determine if the variables measured during the cruise were representative of mean conditions.

A common feature observed on each transect in each season was a very strong gradient in SST across the equatorial front (Fig. 3). During the fall seasons, the

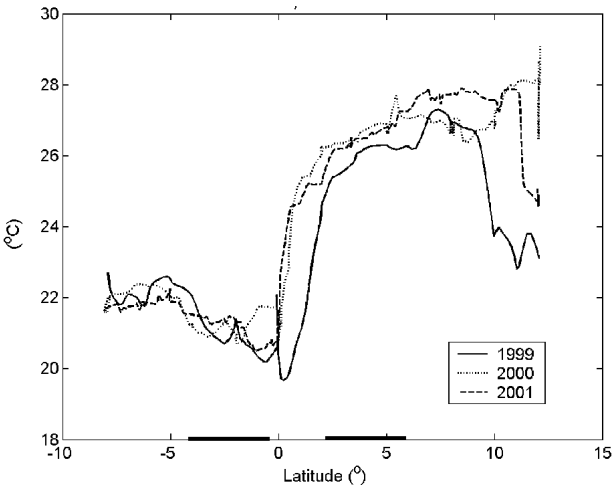

FIG. 3. SST vs latitude for the fall cruises along 95°W. The black (cold) and gray (warm) horizontal lines along the x axis indicate the latitudinal bands where soundings were grouped relative to the SST gradient for compositing.

SST was about 5°–6.5°C warmer at 5° latitude than at the equator on the 95°W transect. The SST gradient was especially large just north of the equator; here, the SST changed by ~4°C in a meridional distance of only 50 km.

To describe the mean ABL structure and its evolution, average (or composite) soundings were created. The method of analysis that follows was applied to each fall transect. Soundings were grouped by location relative to the SST gradient. The cold side of the gradient was generally between 4°S and the equator, while the warm side of the gradient generally ranged from 2° to 6°N. For example, during the fall of 1999, there were eight soundings located on the cold side of the SST gradient and four soundings on the warm side of the gradient. Composite profiles for each group were calculated. The compositing was done by subjectively determining the height of the base of the inversion that caps the boundary layer for each sounding and then nondimensionalizing the vertical coordinate for each sounding by dividing the height by the inversion height (e.g., Albrecht et al. 1995). The use of the nondimensional height helps preserve features of the boundary layer structure, such as the capping inversion that would be smeared out by the averaging process. The soundings in each group were then averaged together. Finally the dimensional height coordinate was restored by multiplying the vertical coordinate by the average inversion height (the average of all the inversion heights in the group). While the integrity of the inversion layer was not preserved, it should not have a great impact overall on the analysis. Composited values of the thermodynamic variables θ, θ_e, and θ_{es} as well as mixing ratio (r), v, and u can then be used to analyze the boundary layer profiles for each transect for all seasons.

The National Center for Atmospheric Research (NCAR) Column Radiation Model (CRM), which is the stand-alone version of the column radiation code used in the NCAR Community Climate Model, was used to calculate the net radiation used in formulating an enthalpy budget that is described in greater detail in section 5.

3. General characteristics of the CTIC region for 1999–2001

Data from November 1999–2001 mean SST and anomalies (TAO Project Office; available online at http://www.pmel.noaa.gov/tao/index.shtml) gives some insight into the overall state of the eastern Pacific Ocean during each cruise. The cold tongue extended the farthest west in November 1999 and was also well developed as evidenced by over −2°C anomalies extending from 110° to 140°W. Cold anomalies extended from 5°S to 10°N across 95°W. Although cold anomalies were also found during November 2000, they were not as strong as during 1999. November of 2001 featured very small anomalies over most of the eastern Pacific basin with the greatest cold anomalies (~ −1°C) near 95°W from around 5°S to the equator. The National Centers for Environmental Prediction (NCEP) Climate Prediction Center (CPC) has subjectively classified El Niño (warm) and La Niña (cold) episodes by season based on reanalyzed SST. From their classification, the late fall of 1999 was classified as a moderate cold episode followed by a weak cold episode in the late fall of 2000. Not until the late fall of 2001 was the Pacific basin in a neutral condition. This classification is consistent with the SST anomalies observed during the 3-yr time period.

Measurements from the *RHB* give a snapshot of the conditions during each of the cruises. Each transect required 8–10 days to complete. Overall, similar features were observed during each cruise, especially the sharp increase in SST over the equatorial front; however, there are some interannual and spatial differences. The SST measurements (Fig. 4a) indicate that all years have a similar structure south of the equator, with near 22°C temperatures observed at the southernmost extent of each transect. SSTs were fairly constant until about 3°S, where a gradual decrease begins signaling the approach toward the coolest waters of the cold tongue. During 2000 and 2001, the rapid increase in SST across the equatorial front begins at the equator while in 1999, the SST does not increase until slightly north of the equator. The difference is due to the propagation of tropical instability waves along the equatorial front that cause the position of the equatorial front to meander north and south of its mean position. The amount of increase across the gradient in each year is similar, about 6°C. During 1999, the SSTs were less than those in the following years north of the equatorial front and actually decreased by ~2°C around 10°N, as a result of jet flows

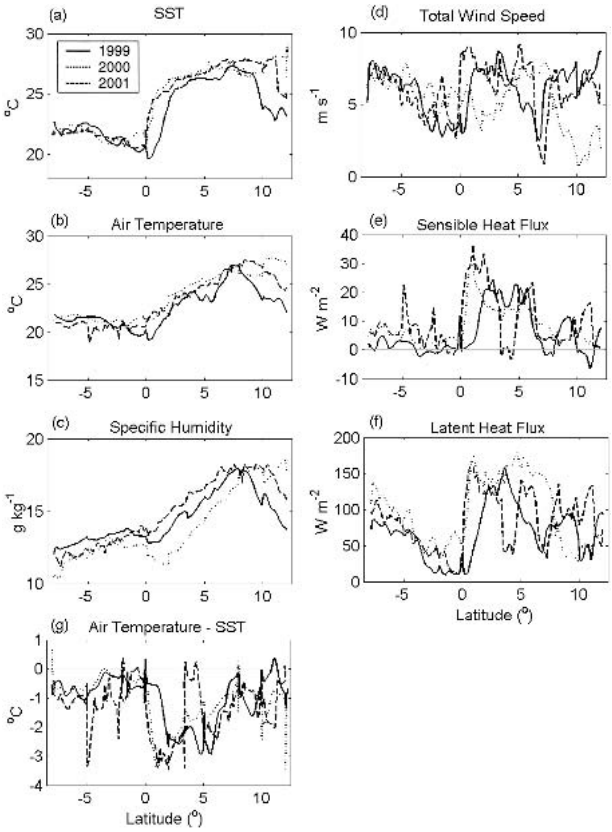

FIG. 4. Ship measurements for the 1999–2001 fall seasons along 95°W.

through the mountain gaps. These variations in the SSTs are consistent with the anomalies shown in the large-scale SST patterns.

Over the cooler waters south of the equator, air temperatures are fairly constant until the underlying waters begin to cool as the cold tongue is approached. Air temperatures (Fig. 4b) are fairly consistent from year to year, with 2001 being slightly cooler than 1999 and 2000 south of the cold tongue. As air crosses the equatorial front and SST gradient, air temperatures begin to increase, but not as sharply as the increase in SST. Over the cooler waters south of the equator, the air–sea temperature differences were fairly small, with the air only slightly cooler than the surface waters. The air–sea temperature difference becomes more substantial after the sharp increase in SST, which leads to a more unstable boundary layer. Slight interannual variations are present north of the cold tongue, with 2000 having the highest overall temperatures and 1999 having the lowest overall temperatures. The specific humidity (q) (Fig. 4c) increases from south to north. South of the cold tongue, the MABL in 1999 is slightly moister than the other two years with q values near 12 g kg^{-1}. However, as the SST gradient is crossed, interannual differences become more clear. The values of q during 2000 are about 3 g kg^{-1} less than for 2001, which has the highest values of q north of the cold tongue. The composite soundings for each year, which will be discussed in a later section, show a similar dryness for 2000.

The wind speed is quite variable from year to year (Fig. 4d); however, there are some consistent features. Wind speeds are on the order of 7 m s^{-1} near the southernmost extent of the transects. Wind speeds begin to gradually decrease as the coolest waters of the cold tongue are approached. As air flows over the equatorial front, the wind speeds tend to increase, although not always at the same rate. In 2000, the wind speeds tend to increase fairly slowly, but for 1999 and 2001, especially, a sharp increase in wind speed is observed in conjunction with the sharp SST gradient. Wind speeds tend to be high north of the SST front, but with considerable variability, especially in the region of the ITCZ between roughly 8° and 12°N. Most of the rapid wind variations are due to aliasing of temporal/spatial structures, not persistent spatial structures.

Sensible heat fluxes south of the SST gradient are quite small (Fig. 4e) and are less than 10 W m^{-2}. Sensible heat fluxes increase rapidly as air passes over the SST gradient, as a result of both increasing SST and a general increase in surface wind speed. Values near 30 W m^{-2} are approached as both the air–sea temperature difference grows larger and wind speeds remain fairly high. There are some variations in the sensible heat flux over the warmer waters north of the SST gradient due principally to variations in the wind speed. Both the sensible and latent heat fluxes were calculated using the sea temperature at a depth of 5 m, except north of the equator in 2001 where the 0.05-m-depth temperature was used. A decrease of ~3°C around 4°N in the 0.05-m depth temperature corresponds to a decrease in the same area in the sensible heat flux. Thus some of the variability in the sensible heat flux can be attributed to the more variable 0.05-m skin SST measurements.

Latent heat fluxes over the extreme southern portions of the transect (Fig. 4f) are generally near 100 W m^{-2}. But as the wind speed decreases toward the cold tongue, these fluxes begin to decrease to less than 50 W m^{-2}. A dramatic increase in the latent heat flux, similar to the one seen in the sensible heat flux, occurs across the equatorial front. As with the sensible heat flux, variability in the latent heat flux is primarily due to variability in the wind speeds as well as variability in the skin temperature used to calculate the heat fluxes.

Daily data from the TAO buoys along 95°W were averaged for the length of each cruise for comparison with the ship-measured data to determine how well the averages from the moving ship represent the multiday averages along the transect. Averages for the fall (1999–2001) seasons were calculated from the TAO buoy data as well as from the ship data (Fig. 5). There is general agreement between the buoy measurements and the ship measurements with a few exceptions. The ship-measured specific humidity is consistently less than the specific humidity measured by the TAO

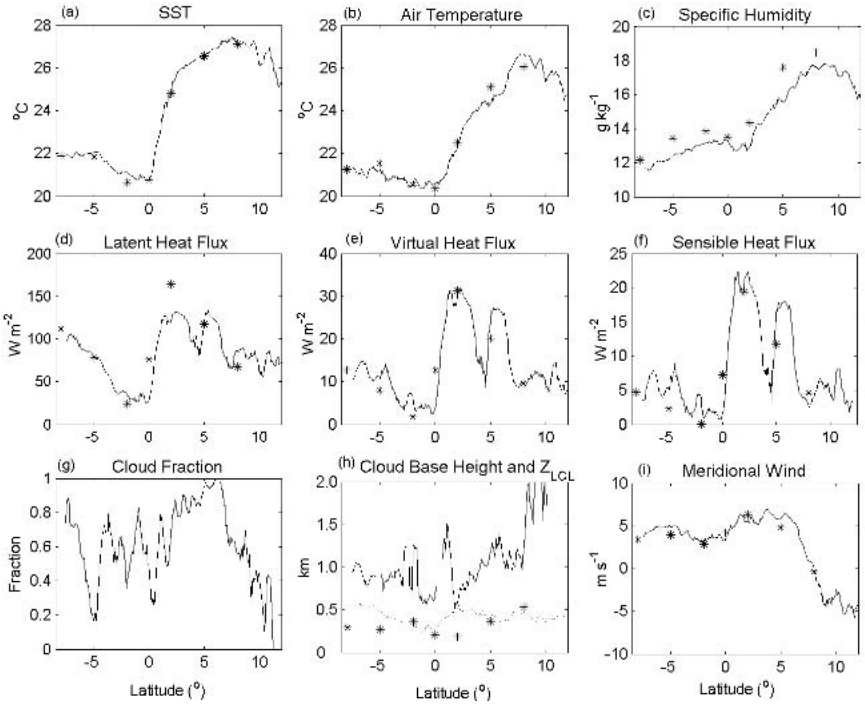

FIG. 5. (a)–(i) Averages for the fall seasons of 1999–2001 of ship observations (lines) and TAO buoy data (stars) along 95°W. In (h), the solid line is the ship ceilometer cloud-base height, and the dashed line represents the z_{LCL} calculated from the ship data; the stars represent the z_{LCL} calculated from the TAO buoy data.

buoys. There is a similar bias in the relative humidity measurements. The difference between these measurements is principally due to near-surface vertical gradients and differences in the heights from which the buoy and ship measurements were made. The fluxes from the ship, however, are comparable with those calculated from the buoy data. The virtual heat flux was calculated to determine the contributions of the sensible and latent heat fluxes to the buoyancy flux. The virtual heat flux is small over the cold tongue but remains positive (upward) and increases across the SST front. Despite sampling different latitudes each day, the ship data provide a reasonable characterization of the average conditions at all latitudes for the cruise periods.

4. Boundary layer evolution

An overall view of the MABL conditions along 95°W is possible with latitudinal cross sections of θ, r, u, and v averaged over 1999–2001 for the fall season (Fig. 6). A decrease in inversion strength is observed from south to north as well as warming at the surface in the same direction. Moisture increases from south to north not only at the surface, but throughout the MABL. The MABL reaches its peak in moisture from 4° to 6°N, with slight drying at the top of the layer north of 6°N. In the zonal direction, light easterly winds dominate at the surface, decreasing to zero near 5°N. A core of strong easterly winds approaching 9 m s^{-1} at 1.6 km is observed from 8° to 10°N. Strong southerly wind components with maximum strength near 500 m extend north of the equator where the winds begin to slacken and eventually become weak and from the north. Above the inversion, a northerly wind component is observed with a stronger core from the equator to 7°N. This low-level meridional circulation has been well documented by Zhang et al. (2004) using the TAO ship soundings.

As the boundary layer air is advected from the cooler waters of the cold tongue to the warmer waters north of the equatorial front, changes occur in the structure of the layer. The composite profiles created for the cold (4°S–0°) and warm (2°–6°N) sides of the front (Figs. 7 and 8) are useful in identifying the specific changes in temperature, moisture, and wind profiles as well as examining both spatial and interannual variations in the MABL structure and its evolution.

The composite profiles of potential temperature for 1999–2001 show a destabilization of the MABL from the cold to the warm side of the SST front (Fig. 7). The height of the inversion increases by about 400 m, and the strength of the inversion also weakens. The θ profiles for the cold side of the SST front show a weak stable layer at 300–400 m (at z_{LCL}) above the surface in all years except for 1999, where the layer from 200–500 m is stable but a shallow, unstable surface layer is observed. The strongest mean inversion structure was ob-

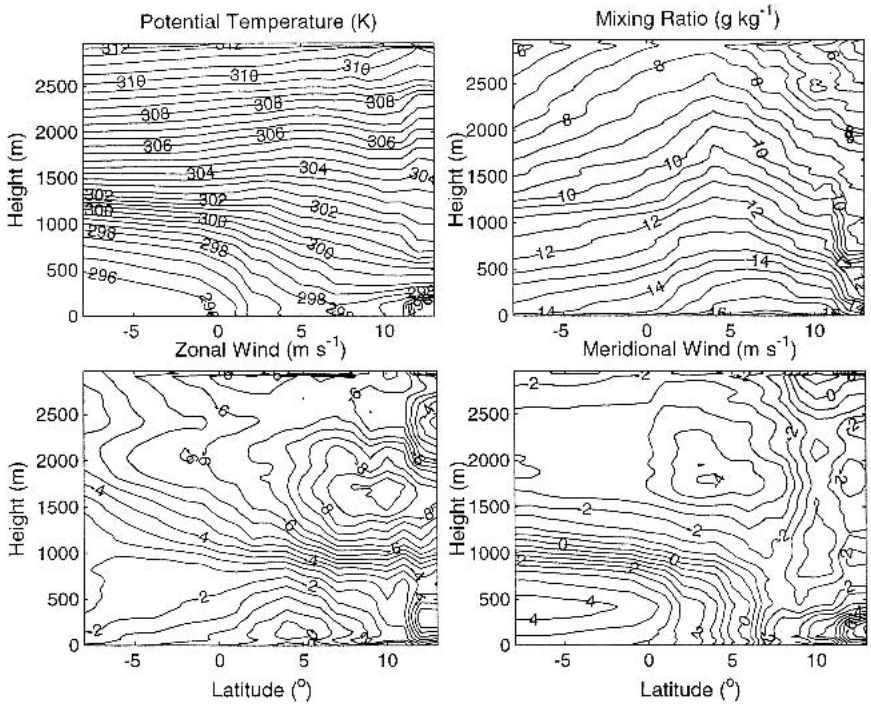

FIG. 6. North–south cross section of the average of fall seasons (1999–2001) along 95°W.

served in 2000, where a decoupling between the subcloud layer and the cloud layer is indicated by a well-defined inversion at 400 m. The temperature above the main capping inversion is about 5 K higher in this year compared with the two other years, and the mixing ratio at this level is 5–10 g kg^{-1} less than the other years. These features could be due to enhanced subsidence during the period of observations. On the warm

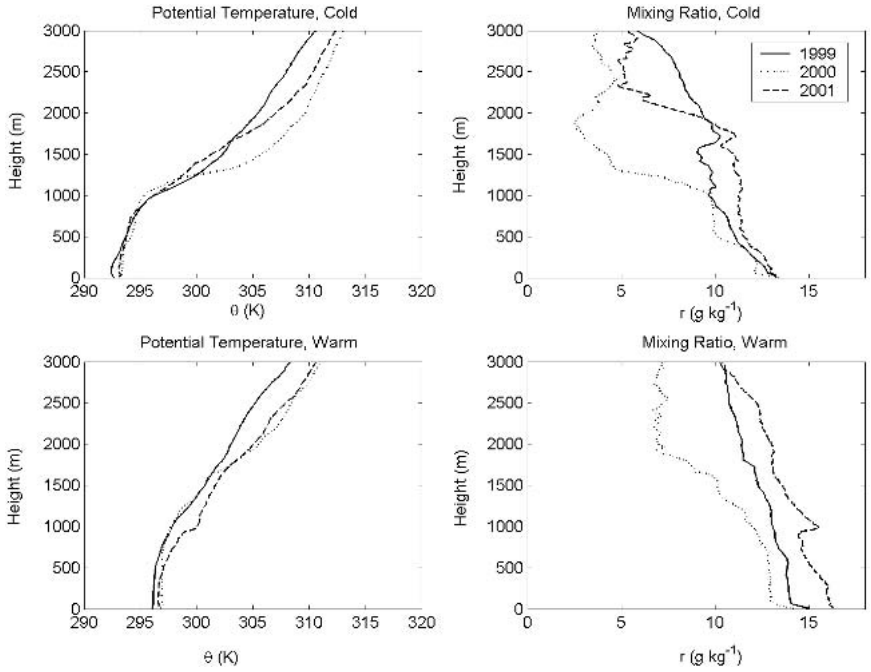

FIG. 7. Composite soundings for the fall seasons of 1999–2001 along 95°W: (left) potential temperature and (right) mixing ratio; (top) the cold (4°S–0°) side of the SST gradient and (bottom) the warm (2°–6°N) side of the gradient.

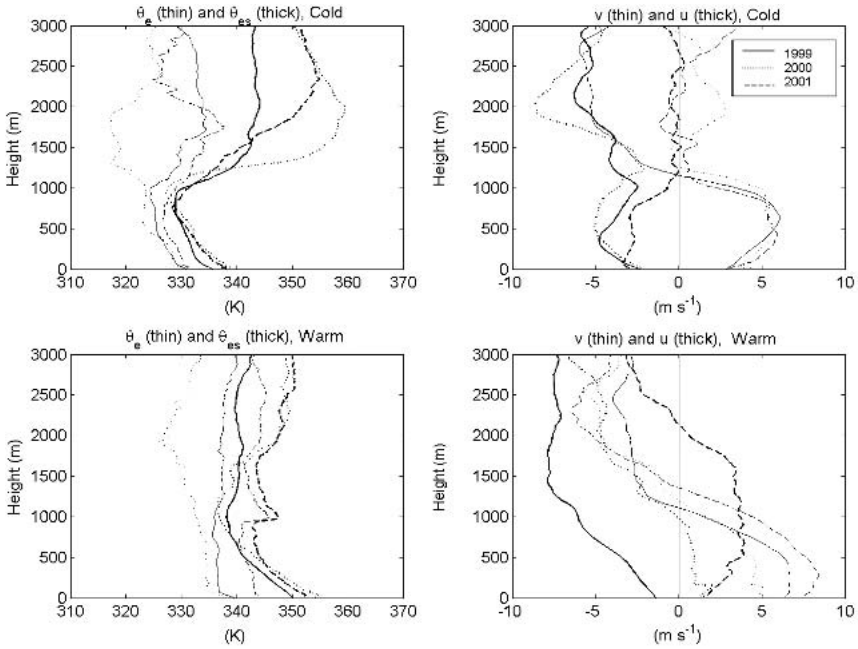

FIG. 8. Composite soundings for the fall seasons 1999–2001 along 95°W: (left) θ_e and θ_{es}, and (right) u and v; top two panels are from the cold (4°S–0°) side of the SST gradient and the bottom two panels are from the warm (2°–6°N) side of the gradient.

side of the front, a fairly well mixed layer extends above the surface in all years. The surface θ increases by 4 K across the SST front. Slightly warmer temperatures were observed during 2000 near the surface.

The surface mixing ratio on the cold side of the front is about 13 g kg^{-1} for all years. Above the inversion, the moisture structure is quite variable from year to year with 2000 being nearly 10 g kg^{-1} drier. The mixing ratio profile shows a moistening at the lower levels on the warm side of the SST front with surface values ranging from 14 to 16 g kg^{-1}. The mixing ratio for 2000 is again drier than the other 2 yr, especially above the MABL, suggesting enhanced subsidence. The warmer temperatures and drier air at the surface observed on the warm side of the front in 2000 are consistent with the ship measurements of these variables.

Profiles of θ_e and θ_{es} can be used to evaluate thermodynamic stability, which can then identify where shallow convective clouds may be able to develop. Positive buoyancy by itself does not guarantee cloud formation; there must be some type of forcing to initiate the process. Consider an air parcel from near the surface that is lifted with constant θ_e. The θ_e and θ_{es} profiles (Fig. 8) on the cold side of the front indicate that parcels rising without entrainment from near the surface would experience an area of positive buoyancy (virtual effects neglected) from about 500 m to the height of the trade inversion, which is near 1200 m in all years [$\theta_{e(sfc)} > \theta_{es}$ from 500 to 1200 m]. This thermodynamic structure would support fair-weather cumulus types of clouds. A similar analysis on the warm side of the front indicates nearly neutral conditions in all years. Some very shallow cumulus-type convection may be possible in 2001, as indicated by the composite profile. These profiles indicate that clouds observed in this area are forced by mixing associated with strong surface fluxes. Although the SST reaches a maximum just north of the equatorial front, air temperature and moisture continue to increase with a maxima occurring near 8°N. The nearly neutral conditions observed on the warm side of the SST front become unstable as both surface moisture and temperature increase, thus increasing θ_e, which was observed in some individual soundings over the ITCZ.

On the cold side of the front, the meridional wind component (Fig. 8) is from the south near the surface between 2.5 and 4.5 m s^{-1}, with the year 2000 exhibiting the strongest surface velocities. The maximum southerly wind occurs at about 500 m with a magnitude of 5–6 m s^{-1}. Just above the inversion, the southerly winds decrease and in some cases switch to northerly, such as in 1999. On the warm side of the front, surface winds are southerly and speeds range from 4.5 to 7.5 m s^{-1}. The maximum southerly wind occurs at 250 m in 2000 and 2001. In 1999, the meridional wind component is fairly well mixed from the surface to about 500 m. Above this level, it begins to decrease and finally shifts to a weak northerly flow. In 2000 and 2001, the meridional component switches to a northerly flow, which was also observed in Zhang et al. (2004), but at a higher altitude above the inversion than in 1999.

The zonal wind component on the cold side of the

front is easterly at the surface in all years. In 2001, the zonal wind decreases with height to near zero at 1200 m. In 1999 and 2000, zonal winds remain easterly throughout the boundary layer and above with speeds reaching up to 8 m s^{-1}. On the warm side of the front, the zonal wind in 1999 is easterly at the surface and remains easterly with height. In 2000 and 2001, from the surface to 1000 and 2100 m, respectively, the zonal wind is westerly. This is consistent with the Coriolis effect, which causes a rightward deflection of the wind as it crosses the equator, as well as zonal pressure gradients caused by convection over Central and South America. Farther north, the zonal wind does become easterly with maximum speeds of generally less than 5 m s^{-1}.

Ceilometer data collected from the ship provides estimates of both cloud fraction and average cloud-base height. Cloud fraction tended to be most variable south of the equator in all years except during the 2001 transect (Fig. 9) and indicates patchy cloudiness. Cloud fractions north of the equatorial front were more constant and were generally high, at or above 0.8. Variations from year to year are probably due to synoptic variability and differences in the location of the equatorial front, which meanders as a result of tropical instability waves. Cloud-base height (Fig. 10) tends to be quite variable with latitude, but generally the highest cloud bases are found over the warmer waters north of the SST front. Over the cold tongue area, the boundary layer tends to be more decoupled as shown by differences between the LCL and cloud-base height. As surface fluxes increase across the SST gradient, the coupling to the surface becomes stronger, and the LCL and cloud-base heights are closer to the same values. Averages of both cloud fraction and cloud-base height were calculated for each side of the SST front for each transect in each season. Tables 1 and 2 give average values for cloud fraction and cloud-base height, respectively. In the fall seasons, the cloud fraction was lower on the cold side of the front and higher on the warm side of the front, except for fall of 2001. This is consistent with a study by Deser et al. (1993) who found "a strong association between visible cloud and the SST waves, with enhanced (reduced) cloudiness in the warm troughs (cold crests) of the waves." Average cloud-base heights tend to increase across the SST front, with the largest increase across the front occurring in 1999.

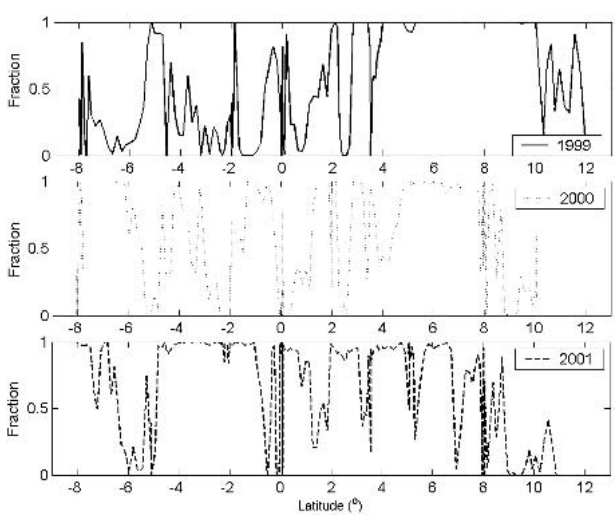

FIG. 9. Ceilometer-measured cloud fraction for fall seasons.

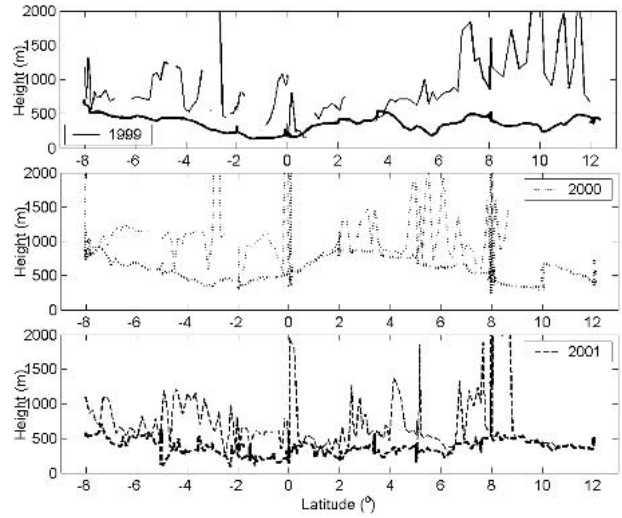

FIG. 10. Ceilometer-measured cloud-base height (thin) and LCL (thick) for fall seasons along 95°W.

Composites of satellite-derived values of cloud fraction and cloud-top height (Figs. 11 and 12) were created to give a broader view of the time evolution of these cloud properties. The maximum values of cloud fraction varied little during the duration of the cruises and were observed north of the equator from about 0° to 7°N (Fig. 11). Sharp gradients can be found on either side of the highest values of cloudiness. The highest time variation of cloudiness is observed south of the equator and is consistent with the patchy cloudiness observed from the ceilometer observations. The satellite-derived cloud-top heights (Fig. 12) south of 6°N are consistently less than about 2 km, while the highest cloud tops, which indicate deeper convection, are observed farther north of the equator, especially around 8°–12°N. These cloud heights are consistent with a strong inversion over the coldest waters that weakens across the equatorial front northward toward the ITCZ.

TABLE 1. Average cloud fraction calculated from ceilometer

	95°W – cold (4°S–0°)	95°W – warm (2°–6°N)
Fall average	0.52	0.87
Fall 1999	0.31	0.99
Fall 2000	0.33	0.78
Fall 2001	0.92	0.83

TABLE 2. Average cloud-base height calculated from ceilometer and LCL calculated from ship measurements (in parentheses) in meters.

	95°W – cold (4°S–0°)	95°W – warm (2°–6°N)
Fall average	809 (310)	988 (523)
Fall 1999	580 (221)	1088 (404)
Fall 2000	1148 (428)	1163 (803)
Fall 2001	699 (281)	712 (363)

A comparison of ceilometer and satellite composites (Fig. 13) shows overall good agreement between the two methods for estimating fractional cloudiness. A comparison of the composite satellite cloud-top height and inversion heights from the soundings shows fairly good agreement over the cold tongue region (Fig. 14). In the ITCZ region, the agreement is not as good, which could be attributed to several cloud layers at various heights where the satellite is observing the highest cloud layer, not the cloud layer associated with the boundary layer. This comparison confirms that the transect results are a representative sample of the MABL clouds within a much larger area than the narrow line of the transect. Conversely, they provide a partial validation of the satellite retrievals of cloud fraction and cloud height in the CTIC region.

For a broad look at the changes in boundary layer structure across the equatorial front, a composite sounding was created by averaging the three composite soundings for the fall seasons of 1999–2001 for both the cold (4°S–0°) and warm (2°–6°N) sides of the gradient (Fig. 15). A weighted average of the composites from each year showed only slight differences from the unweighted average, and the unweighted average was used. The difference in θ and q with height from the warm to the cold side of the gradient is shown in Fig. 16. The $\Delta\theta$ profile is fairly constant to about 1000 m followed by a decrease toward the base of the inversion. However the Δq profile, has a more varied structure, with an increase in the average mixing ratio from ~2 g kg^{-1} increasing to ~3 g kg^{-1} at 500 m. The virtual potential temperature (θ_v) for both sides of the gradient and the difference between the two can be seen in Fig. 17. The destabilization of the boundary layer is quite evident, with $\Delta\theta_v$ decreasing with height especially in the inversion layer. The destabilization of the inversion results from a warming of the boundary layer and a corresponding cooling above the inversion. The source of this cooling may be associated with reduced subsidence over the warm waters compared with that over the cold tongue. Below the inversion, there is a general destabilization as the lower part of the layer warms above 1°C relative to the top of the layer. Thus the mean virtual temperature lapse rate in the MABL decreases by about 1°C km^{-1} and is consistent with the destabilization first discussed by Wallace et al. (1989). A similar composite and difference was made for the total wind speed (Fig. 18). Surface winds increase by about 2 m s^{-1} from the cold to the warm side of the equatorial front, while wind speeds are lower throughout most of the boundary layer on the warm side of the front. This is consistent with the mixing hypothesis of Wallace et al. (1989), where enhanced mixing on the warm side of the equatorial front causes surface wind

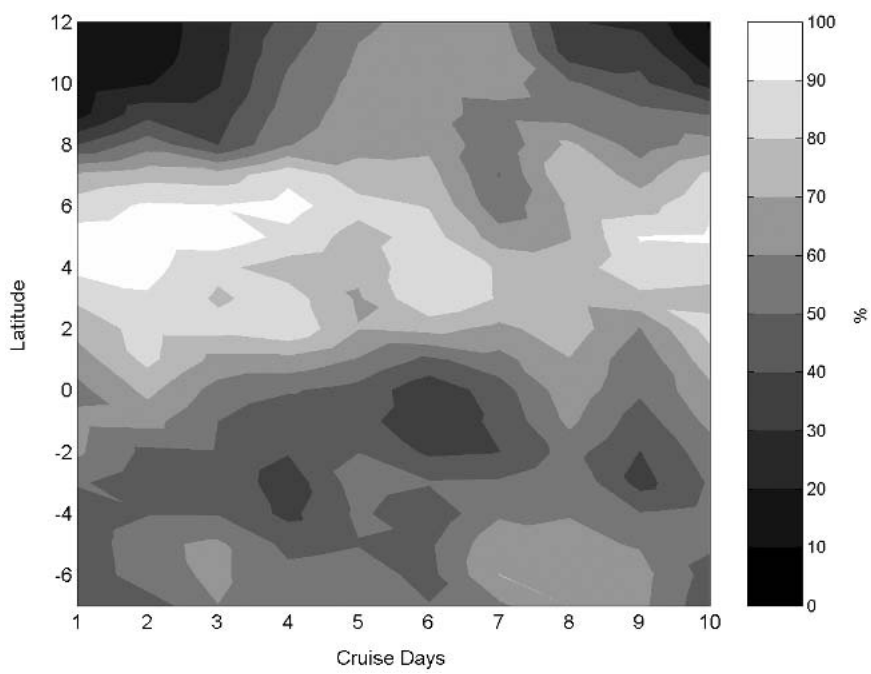

FIG. 11. Satellite-derived cloud fraction composite for 1999–2001 along 95°W.

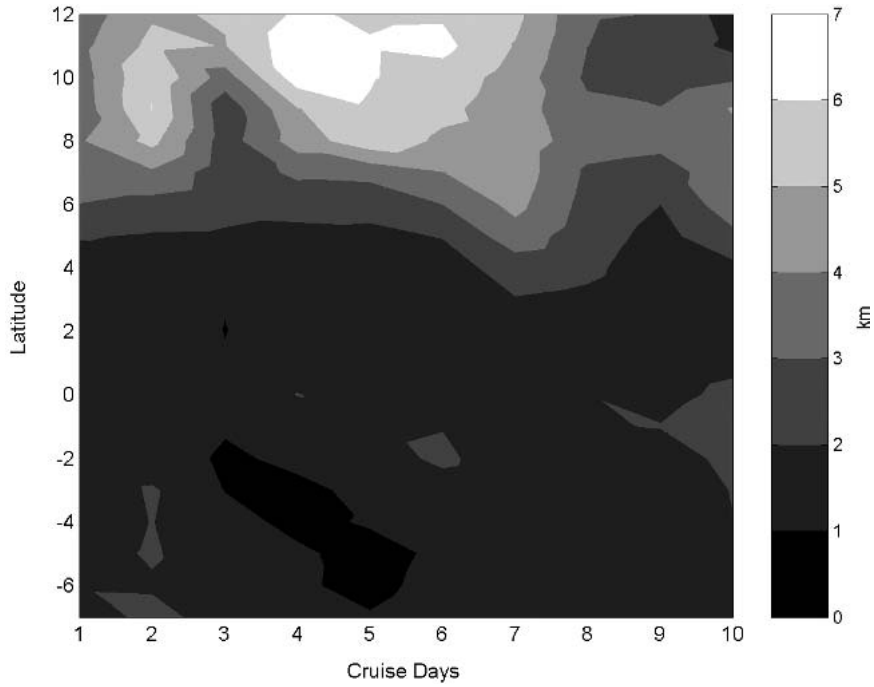

FIG. 12. Satellite-derived cloud-top height composite for 1999–2001 along 95°W.

speeds in that area to increase. The data in these overall composite soundings will be used in the next section in formulating energy and moisture budgets.

5. Energy and moisture budgets

In the previous section, both the structure and the evolution of the MABL across the cold tongue were discussed. To better understand the roles of various physical processes occurring during the MABL evolution, energy and moisture budgets were created. Equations (1) and (2) are the budget equations used in this analysis (following Stull 1988):

$$\left(\frac{d\overline{\theta}}{dt}\right)_{\mathrm{Hor}} = -\overline{w\frac{\partial\theta}{\partial z}} - \frac{1}{\rho c_p}\frac{(F_{\theta_l})_{z_B} - (F_\theta)_o}{z_B} + Q_R \quad (1)$$

and

$$\left(\frac{d\overline{q}}{dt}\right)_{\mathrm{Hor}} = -\overline{w\frac{\partial q}{\partial z}} - \frac{1}{\rho L_v}\frac{(F_{q+l})_{z_B} - (F_q)_o}{z_B}, \quad (2)$$

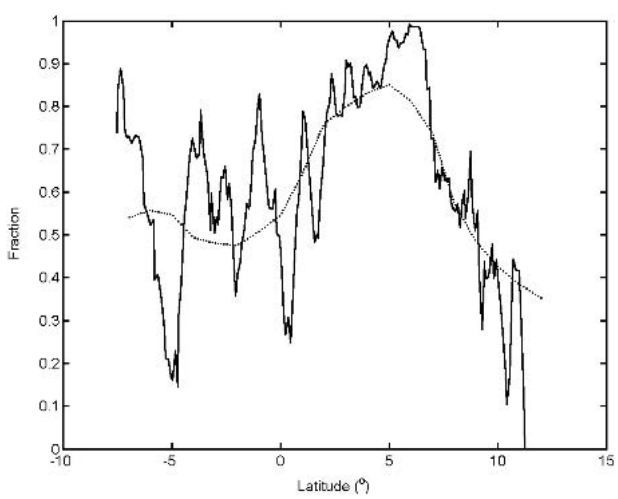

FIG. 13. Ceilometer (solid) and satellite (dashed) composite comparison of fractional cloudiness 1999–2001 along 95°W.

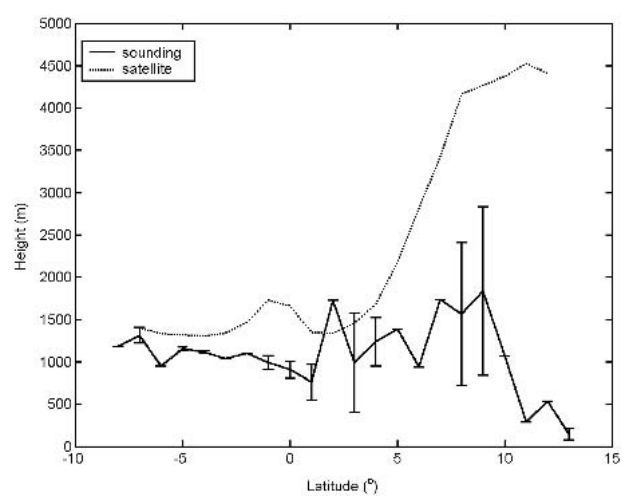

FIG. 14. Inversion heights from soundings (1999–2001) and satellite cloud-top height composite along 95°W. Error bars are the standard deviation of the average inversion height in each latitude bin.

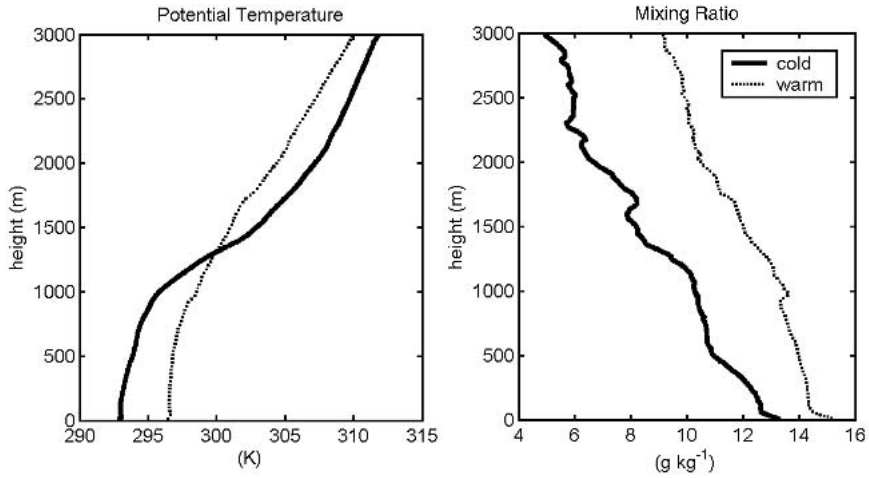

FIG. 15. Composite soundings for the cold (4°S–0°) and warm (2°–6°N) sides of the SST gradient for the fall seasons from 1999 to 2001 along 95°W; (left) potential temperature and (right) mixing ratio.

where the depth average is defined as

$$\frac{1}{z_B}\int_0^{z_B}(\ )dz,$$

where $\overline{\theta}$ and $\overline{q}$ represent the mean value averaged through the boundary layer, z_B is the depth of the boundary layer, c_p is the specific heat of air, L_v is the enthalpy of vaporization of water, w is the vertical velocity, F_{θ_l} is the heat flux (where θ_l is the liquid water potential temperature that allows the effects of liquid water to be accounted for), F_{q+l} is the moisture flux including liquid water, and Q_R is the radiative heating/cooling rate averaged over the depth of the boundary layer. The terms on the left-hand sides of Eqs. (1)–(2) represent the total horizontal derivative of $\overline{\theta}$ and $\overline{q}$, and the vertical advection term is included as the first term on the right-hand side of each equation. To simplify the analysis, it is assumed that the horizontal advection is zero in the zonal direction. The subcloud differences in θ and q between 95° and 110°W are 1 K and 0.5 g kg^{-1}, respectively, which is substantially less than the north–south gradient. This assumption allows the total derivative to be applied to the meridional component of the wind.

The radiative source term was calculated using the NCAR CRM (Kiehl et al. 1996). The composite profiles of temperatures and moisture as a function of pres-

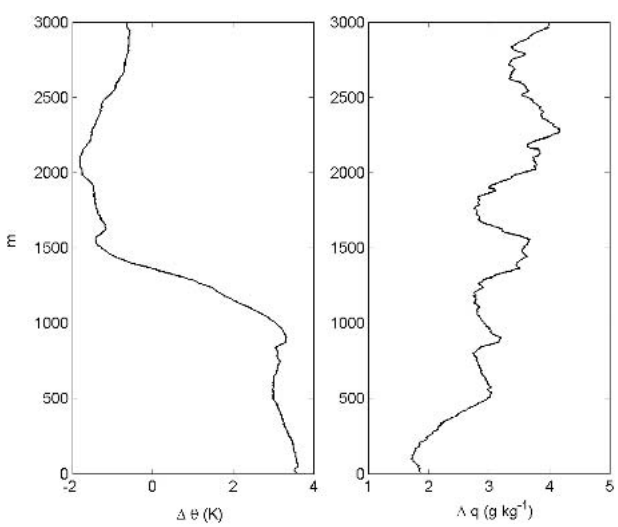

FIG. 16. Difference in (left) potential temperature and (right) mixing ratio between warm and cold composites for 1999–2001 fall seasons along 95°W.

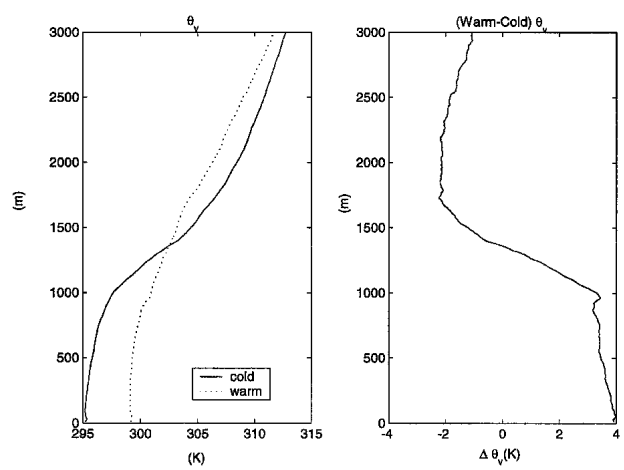

FIG. 17. Composite (1999–2001) of (left) virtual potential temperature on cold and warm sides of the equatorial front and (right) the warm-minus-cold difference of virtual potential temperature along 95°W.

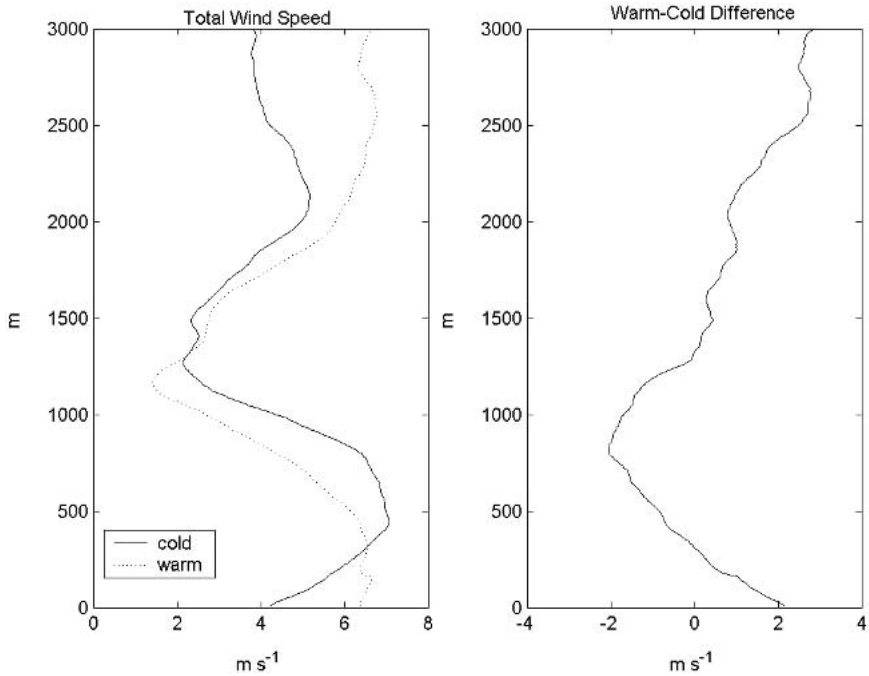

FIG. 18. (left) Composite total winds speed for 1999–2001 for the warm and cold sides of the equatorial front and (right) the warm-minus-cold wind speed difference along 95°W.

sure were used as input up to 750 hPa; above this level, the annual values at 15°N from the *U.S. Standard Atmosphere Supplements, 1966* were used to provide upper-level values. The model allows for cloudy layers, and a typical value of liquid water content (LWC) of 0.3 g m^{-3} (Miles et al. 2000) was used for the model. Cloud base and cloud top were specified at 740 and 1210 m, respectively, for the Q_R estimates. The model was run at noon local time (to calculate the maximum shortwave heating), and the daily average net radiation was estimated using weighted shortwave and longwave heating rates. Under the cloud conditions observed along the 95°W transect, the radiative heating of the boundary layer, averaged from the top of the inversion to the surface, $(Q_R)_o$, was calculated to be -1.7 K day^{-1}; Q_R in Eq. (1) is the radiative heating averaged from the surface to the inversion. Since the mean fractional cloudiness (β) is observed to be about 0.8, a simple partitioning of the radiative cooling between the inversion layer and that below cloud top is assumed following the approach used by Albrecht et al. (1979). To determine how sensitive the net radiation over the depth of the boundary layer was to cloud cover, a clear-sky average was calculated as $Q_R = -1.5$ K day^{-1}, about a 10% decrease in the net radiation relative to the cloudy case. Further treatment of the radiative terms will be given below, and the sensitivity of the budget to changes in the net radiation will be discussed.

To formulate the budget several types of data were used. The composite soundings created (Fig. 15) from the 1999–2001 data were used to calculate the vertical gradients of θ and q by using average values from the cold and warm composite soundings. Average north–south cross sections of the latent and sensible heat fluxes, as well as cloud fraction, cloud-base height, SST, air temperature, and meridional wind were calculated for 1999–2001 from 8°S to 12 N° across the CTIC as shown in Fig. 5. The modification of the MABL is assumed to begin with a sharp increase in SST at the equator as seen in Fig. 5. Although the composite soundings result from composites calculated from ~4°S to 0° (cold), starting the budget calculation at the equator can be justified as a result of the relative consistency of SST and small surface fluxes just south of the cold tongue. The meridional wind is used to determine the amount of time required for a parcel of air to travel from the equator to 5°N. This approach assumes that this area (0°–5°N) is where the major MABL modification occurs, including rapid increases in surface fluxes. Thus, this is the area where the budget calculations can be most useful in noting the physical processes that contribute to this modification. The sensible and latent heat fluxes used in the budget analysis were the average value of these fluxes calculated from 0° to 5°N. The fluxes along the north–south transects provide a means to evaluate the enthalpy, moisture, and mass budgets and to estimate the average fluxes needed at the top of the MABL to balance the budgets. The vertical velocity (w) was estimated using $w = -Dz$ integrated from the surface to the top of the MABL, where D is the assumed large-scale divergence.

The vertical gradients in the first term on the right side of Eqs. (1)–(2) were approximated as follows:

$$\frac{\partial q}{\partial z} = \frac{q_{z_B} - q_o}{z_B} = \gamma_q \quad \text{and} \tag{3}$$

$$\frac{\partial \theta}{\partial z} = \frac{\theta_{z_B} - \theta_o}{z_B} = \gamma_\theta. \tag{4}$$

The depth of the boundary layer was assumed to vary linearly with time, where

$$z_B = z_{B_o} + \alpha(t - t_o), \tag{5}$$

and

$$\alpha = \frac{z_{B_f} - z_{B_o}}{t_f - t_o}.$$

Equations (1) and (2) are integrated in time from t_o to t_f. The vertical velocity, w, is assumed to be an average over the depth of the MABL. Equations (6) and (7) are the time-integrated budget equations as follows, with brackets denoting average values from 0° to 5°N:

$$\begin{aligned}\overline{\theta}_f - \overline{\theta}_o = {} & -w[(\gamma_\theta)(t_f - t_o)] - \frac{1}{\rho c_p}\frac{[(F_{\theta_l})_{z_B}]}{\alpha} \\ & \ln\left[1 + \frac{\alpha}{z_{B_o}}(t_f - t_o)\right] + \frac{1}{\rho c_p}\frac{[(F_\theta)_o]}{\alpha} \\ & \ln\left[1 + \frac{\alpha}{z_{B_o}}(t_f - t_o)\right] + (1 - \beta)(Q_R)(t_f - t_o)\end{aligned} \tag{6}$$

and

$$\begin{aligned}\overline{q}_f - \overline{q}_o = {} & -w[(\gamma_q)(t_f - t_o)] - \frac{1}{\rho L_v}\frac{[(F_{q+l})_{z_B}]}{\alpha} \\ & \ln\left[1 + \frac{\alpha}{z_{B_o}}(t_f - t_o)\right] + \frac{1}{\rho L_v}\frac{[(F_q)_o]}{\alpha} \\ & \ln\left[1 + \frac{\alpha}{z_{B_o}}(t_f - t_o)\right].\end{aligned} \tag{7}$$

The values used in the budget calculations can be found in Table 3. Temperature and moisture fluxes at the top of the MABL were unknown and are found as the residual after the initial budget calculation. Tables 4 and 5 give the results for the energy and moisture budgets, respectively. The conversion from °C day^{-1} to W m^{-2} was made using the average boundary layer depth, z_{avg}.

The results from this budget analysis are consistent with what one would expect in the MABL modification. It is encouraging that the results are physically meaningful; thus, using composite soundings and composite cross sections of fluxes is a valid way to understand the processes important for MABL modification. An increase in both the mean temperature and moisture of the layer occurs across the strong SST gradient. The subsidence terms contribute small amounts of warming and drying. The entrainment term in the θ budget was a significant warming term necessary to balance the radiative cooling term. The surface heat flux term was a warming term as well but is small compared with the entrainment warming. In the q budget, the surface moisture flux was the most significant term contributing to the increase in moisture across the gradient. The entrainment term contributes some drying but is quite small.

TABLE 3. Values used in budget calculations.

D	2×10^{-6} s^{-1}
z_{avg}	1214 m
w	−0.121 cm s^{-1}
$t_f - t_o$	1.01×10^5 s
Q_R	−1.67 K day^{-1}
$\theta_f - \theta_o$	3.8 K
$q_f - q_o$	2.4 g kg^{-1}
$(\gamma_{\theta o})_{\text{avg}}$	0.003 K m^{-1}
$(F_{\theta o})_{\text{avg}}$	14.3 W m^{-2}
$(\gamma_{qo})_{\text{avg}}$	−0.003 g kg^{-1} m^{-1}
$(F_{qo})_{\text{avg}}$	105.1 W m^{-1}
c_p	1005 J kg^{-1} K^{-1}
L_v	2.5×10^6 J kg
β	0.8

The entrainment rate at the top of the MABL can be calculated following Eqs. (8)–(9) (Stull 1988):

$$w_e = -\frac{\overline{w'\theta_l'}}{\Delta\theta} + \frac{\Delta F_R}{\Delta\theta} \quad \text{and} \tag{8}$$

$$w_e = -\frac{\overline{w'q'}}{\Delta q}, \tag{9}$$

where

$$\Delta F_R \propto \beta Q_R z_B, \tag{10}$$

where w_e is the entrainment rate; $\overline{w'\theta'}$ and $\overline{w'q'}$ are the sensible and latent heat fluxes at the top of the MABL, respectively, and $\Delta\theta$ and Δq represent the temperature and moisture jumps across the inversion. Table 6 lists the values ued in calculating the entrainment rates. The entrainment rates calculated from Eqs. (8)–(9), respectively, are 0.32 and 0.13 cm s^{-1}. Typical values of entrainment rates in stratocumulus clouds range from 0.1 to 0.5 cm s^{-1} (Kawa and Pearson 1989). The entrainment rate calculated using the sensible heat flux at the top of the MABL is about 2 times larger than the one calculated with the latent heat flux at the top of the MABL. As a check on the consistency of these results,

TABLE 4. Results from θ budget. Top row units are °C day^{-1}; bottom row units are W m^{-2}.

$(\theta_f - \theta_o)_{\text{avg}}$	Subsidence	Entrainment	Surface heat flux	Radiation
+3.2 =	+0.31	2.4	+0.84	−0.33
+56 =	+5.4	+42	+14	−5.8

TABLE 5. Results from q budget. Top row units are g kg^{-1} day^{-1}; bottom row units are W m^{-2}.

$(q_f - q_o)_{\text{avg}}$	Subsidence	Entrainment	Surface moisture flux
+2.0 =	−0.27	−0.15	+2.5
+88 =	−12	−6.3	+106

entrainment rates can be computed using the following (after Lilly 1968):

$$\frac{dh}{dt} = w_T + w_e, \tag{11}$$

where h is the depth of the MABL, w_e is the entrainment rate, and w_T is the large-scale vertical velocity (w) used in the budget calculations. The entrainment rate calculated from Eq. (11) is 0.50 cm s^{-1}. There are clearly uncertainties in these entrainment rates as a result of the simplified treatment. Both the subsidence and radiation terms were estimated leading to possible uncertainties. This method assumes a thin inversion layer that may also introduce errors because in reality it is finite. The assumption of zero zonal moisture advection may be another source of error. If there were some other moistening processes occurring in addition to the surface moisture flux, the entrainment term would become larger and thus would increase the entrainment rate calculated from the q budget and bring it closer to the rate calculated from the θ budget.

There is some sensitivity in the entrainment rates to both the divergence and the radiative cooling. Tables 7a and 7b give some examples of the sensitivity of each of these parameters. Decreasing the divergence decreases the subsidence, which causes an increase in the magnitude of the entrainment terms from the enthalpy and moisture budgets. This in turn increases the entrainment rate calculated from the sensible heat flux at the top of the MABL and the entrainment rate calculated from the latent heat flux at the top of the MABL. The opposite effect occurs when the divergence is increased. With a divergence of 1.0×10^{-6} s^{-1}, the entrainment rates from the budgets are more comparable in magnitude. When the radiative cooling is decreased to the amount calculated for clear-sky conditions, there is not much effect on the entrainment rate. Although clouds are important for the vertical distribution of radiative heating/cooling (i.e., high values of cooling occurring at cloud top), this effect is minimized in a bulk model such as this. Further decreases in Q_R cause decreases in the sensible heat flux at the top of the MABL, thus decreasing the entrainment rate and large-scale vertical velocity. Increases in Q_R have the opposite effect, causing increases in the flux at the top of the MABL and consequently in the entrainment rate.

TABLE 6. Values used in calculating entrainment rates.

$\Delta\theta$	4.6 K
Δq	−1.6 g kg^{-1}
w_T	−0.0012 m s^{-1}
ΔF_R	−24 W m^{-2}
β	0.8
Q_R	−1.7 K day^{-1}
h_o	1020 m
h_f	1410 m

TABLE 7A. Sensitivity of entrainment rates to changes in divergence with $Q_R = -1.67$ K day^{-1}.

D (s^{-1})	w_e (q) (cm s^{-1})	w_e (θ) (cm s^{-1})	w_e (from dh/dt)
1×10^{-6}	0.25	0.37	0.45
2×10^{-6}	0.13	0.32	0.50
3×10^{-6}	0.012	0.27	0.57

TABLE 7B. Sensitivity of entrainment rates to changes in radiation with $D = 2 \times 10^{-6}$ s^{-1}.

Q_R (K day^{-1})	w_e (θ) (cm s^{-1})
−1.0	0.28
−1.5	0.31
−1.67	0.32
−2.0	0.34

6. Summary

This study of the MABL evolution over the CTIC is unique as a result of the data collected over 3 years that included soundings, ship measurements, and remotely sensed cloud properties. Two states of the eastern Pacific Ocean were observed with cold episodes in 1999–2000 and neutral conditions in 2001. These differing states along with fluctuations in the location of the equatorial front contribute to some of the interannual variations that are observed.

A destabilization of the MABL occurs across the equatorial front during the fall seasons. The strong capping inversion present south of the equator inhibits deep cloud formation. As MABL air is advected northward, it becomes increasingly unstable, with maximum instability caused by surface moistening occurring over the ITCZ due to the finite time required for the MABL to adjust to the sudden increase in SST. Moisture increases throughout the entire MABL across the SST gradient. Increases in surface wind speed were observed across the equatorial front, as well as decreases in the relative humidity. These are consistent with the vertical mixing mechanism proposed by Wallace et al. (1989) described in section 2. One of the most notable areas of interannual variability is in the above inversion moisture structure with a significant drying above the inversion observed in 2000. This result is consistent with the interannual differences in the meridional winds above the inversion. The winds were southerly in 2000 and hence were advecting relatively dry air from the Southern Hemisphere. A temperature variation is also associated with this moisture variation.

Cloudiness tends to be variable over the cooler waters south of the equatorial front ranging from 0.2 to 0.8 coverage. North of the equatorial front, cloudiness becomes more constant with greater than 0.8 coverage until a decrease in the low-level cloudiness is observed near the ITCZ. Cloud-base heights tended to decrease along with the SST to a minimum just north of the equator followed by a steady increase in cloud-base height to the north of the equatorial front as the boundary layer warms and cools. Over the cold tongue, the boundary layer at times is decoupled; as the surface fluxes increase with the SST, the MABL becomes more coupled as evidenced by a close relationship between the LCL and cloud-base heights.

Sensible and latent heat fluxes are small to the south of the equatorial front but increase sharply as both SST and wind speed increase. These fluxes are important in the modification of the MABL, as shown in an analysis using energy and moisture budgets. The results from the budget analysis show that the surface latent heat flux is responsible for the moistening as the boundary layer moves from the cold to the warm side of the SST gradient. This moistening is balanced by subsidence drying as well as entrainment drying. The surface heat flux acts as a warming term. However, the entrainment warming dominates the energy budget. Thus, while the surface fluxes are important in understanding how the MABL changes across the equatorial front, entrainment at the top of the MABL plays an important role as well, although it is less well understood. There are some inconsistencies between the entrainment rates calculated from the θ (0.32 cm s^{-1}) and q budgets (0.13 cm s^{-1}); this difference can be attributed to sampling, uncertainties in the vertical velocity, and other errors. The overall consistency of the budget results reveals that it is promising as a way to understand the roles of various physical processes in the MABL evolution. While a momentum budget was not attempted in this study [McGauley et al. (2004) have undertaken a study of the momentum balances in the region], this type of budget would give another perspective on entrainment rates and add to the overall value of the analysis.

This work has been focused on understanding the MABL structure over the CTIC and how it evolves from the cold tongue northward. Past studies of this area, such as Wallace et al. (1989) and Yin and Albrecht (2000), focused on broader features of the area. Composite soundings from both the cold tongue and ITCZ areas from Yin and Albrecht show similar features to the composite soundings in this study, with a destabilization occurring across the strong SST gradient. The Bond (1992) study examined a single transect in the area and focused mainly on the overall characteristics and mixed-layer variability. The meridional secondary circulation observed in many of the composites was also observed in a study by Zhang et al. (2004) using EPIC aircraft data. Multiple years of data available for this work have allowed interannual variations, as well as seasonal variations to be examined. The availability of cloud data allowed a look at the cloud characteristics of the region and how these characteristics were tied to the strong SST gradient. The use of composites in this study was also instrumental in identifying the changes that occurred in the boundary layer structure across the equatorial front.

A more sophisticated model would be needed to account for the complex vertical moisture structure as well as the vertical distribution of radiation, which may provide for better estimates of entrainment rates. It would be useful to compare the results of budget studies with models to evaluate the existing parameterizations of the region. The distance across the SST gradient from the cold to warm side is about 5° of latitude, which may translate to 2–3 grid points in a model. Similar budget calculations could be done using the model information at each grid point to determine how the model's budget compares with observations. Increasing the accuracy of parameterizations of the CTIC in global models could be helpful in increasing the forecast accuracy of these models, but proper representation of the boundary layer transition across the CTIC will be a challenge for models. Also, more study is needed of the above inversion moisture structure as well as the low-level meridional secondary circulation (e.g., as discussed by Zhang et al. 2004) and what effect it has on the MABL structure.

Acknowledgments. This work was supported by NOAA Grant NA17RJ1226. The satellite analyses were supported by the NOAA PACS Program under NOAA Agreement NA00AANRG0330.

REFERENCES

Albrecht, B. A., A. K. Betts, W. H. Schubert, and S. K. Cox, 1979: A model of the thermodynamic structure of the trade-wind boundary layer: Part I. Theoretical formulation and sensitivity tests. *J. Atmos. Sci.,* **36,** 73–89.

——, M. P. Jensen, and W. J. Syrett, 1995: Marine boundary layer structure and fractional cloudiness. *J. Geophys. Res.,* **100,** 14 209–14 222.

Ayers, J. K., P. W. Heck, A. D. Rapp, P. Minnis, D. F. Young, W. L. Smith Jr., and L. Nguyen, 2002: A one-year climatology of cloud properties derived from GOES-8 over the southeastern Pacific for PACS. Preprints, *11th Conf. on Cloud Physics*, Ogden, UT, Amer. Meteor. Soc., CD-ROM, P2.10.

Bolton, D., 1980: The computation of equivalent potential temperature. *Mon. Wea. Rev.,* **108,** 1046–1053.

Bond, N., 1992: Observations of planetary boundary layer structure in the eastern equatorial Pacific. *J. Climate,* **5,** 699–706.

Cronin, M. F., N. Bond, C. Fairall, J. Hare, M. J. McPhaden, and R. A. Weller, 2002: Enhanced oceanic and atmospheric monitoring underway in the eastern Pacific. *Eos, Trans. Amer. Geophys. Union,* **83,** 210–211.

Deser, C., J. Bates, and S. Wahl, 1993: The influence of sea surface temperature gradients on stratiform cloudiness along the equatorial front in the Pacific Ocean. *J. Climate,* **6,** 1172–1180.

Fairall, C. W., E. F. Bradley, J. E. Hare, A. A. Grachev, and J. B.

Edson, 2003: Bulk parameterization of air–sea fluxes: Updates and verification for the COARE algorithm. *J. Climate,* **16,** 571–591.

Hashizume, H., S. Xie, M. Fujiwara, M. Shiotani, T. Wantanbe, Y. Tanimoto, W. T. Liu, and K. Takeuchi, 2002: Direct observations of atmospheric boundary layer response to SST variations associated with tropical instability waves over the eastern equatorial Pacific. *J. Climate,* **15,** 3379–3393.

Hayes, S. P., M. J. McPhaden, and J. M. Wallace, 1989: The influence of sea surface temperature on surface wind in the eastern equatorial Pacific: Weekly to monthly variability. *J. Climate,* **2,** 1500–1506.

Kawa, S. R., and R. Pearson Jr., 1989: An observational study of stratocumulus entrainment and thermodynamics. *J. Atmos. Sci.,* **46,** 2649–2661.

Kiehl, J. T., J. Hack, G. Bonan, B. Boville, B. Briegleb, D. Williamson, and P. Rasch, 1996: Description of the NCAR Community Climate Model (CCM3). NCAR Tech. Note NCAR/TN-420+STR, Boulder, CO, 152 pp.

Kloesel, K. A., and B. A. Albrecht, 1989: Low-level inversions over the tropical Pacific—Thermodynamic structure of the boundary layer and the above-inversion moisture structure. *Mon. Wea. Rev.,* **117,** 87–101.

Lilly, D. K., 1968: Models of cloud-topped mixed layers under a strong inversion. *Quart. J. Roy. Meteor. Soc.,* **94,** 292–309.

McGauley, M., C. Zhang, and N. A. Bond, 2004: Large-scale characteristics of the atmospheric boundary layer in the eastern Pacific cold tongue–ITCZ region. *J. Climate,* **17,** 3907–3920.

Miles, N. L., J. Verlinde, and E. Clothiaux, 2000: Cloud droplet size distributions in low-level stratiform clouds. *J. Atmos. Sci.,* **57,** 295–311.

Minnis, P., and Coauthors, 2001: A near-real time method for deriving cloud and radiation properties from satellites for weather and climate studies. Preprints, *11th Conf. on Satellite Meteorology and Oceanography*, Madison, WI, Amer. Meteor. Soc., 477–480.

Stull, R. B., 1988: *An Introduction to Boundary Layer Meteorology*. Kluwer Academic, 666 pp.

Wallace, J. M., T. P. Mitchell, and C. Deser, 1989: The influence of sea-surface temperature on surface wind in the eastern equatorial Pacific: Seasonal and interannual variability. *J. Climate,* **2,** 1492–1499.

Weller, R., cited 1999: A science and implementation plan for EPIC. [Available online at http://www.atmos.washington.edu/gcg/EPIC/EPIC_rev.pdf.]

Yin, B., and B. A. Albrecht, 2000: Spatial variability of atmospheric boundary layer structure over the eastern equatorial Pacific. *J. Climate,* **13,** 1574–1592.

Zhang, C., M. McGauley, and N. Bond, 2004: Shallow meridional circulation in the tropical east Pacific. *J. Climate,* **17,** 133–139.